Article

Solution NMR Analysis of Ligand Environment in Quaternary Ammonium-Terminated Self-Assembled Monolayers on Gold Nanoparticles: The Effect of Surface Curvature and Ligand Structure

Meng Wu, Ariane M. Vartanian, Gene Chong, Arun Kumar Pandiakumar, Robert J Hamers, Rigoberto Hernandez, and Catherine J. Murphy

J. Am. Chem. Soc., **Just Accepted Manuscript** • DOI: 10.1021/jacs.8b11445 • Publication Date (Web): 14 Feb 2019

Solution NMR Analysis of Ligand Environment in Quaternary Ammonium-Terminated Self-Assembled Monolayers on Gold Nanoparticles: The Effect of Surface Curvature and Ligand Structure

Meng Wu[†], Ariane M. Vartanian[†], Gene Chong[‡], Arun Kumar Pandiakumar[§], Robert J. Hamers[§], Rigoberto Hernandez[‡], Catherine J. Murphy*[,†]

[†]Department of Chemistry, University of Illinois at Urbana-Champaign, Urbana, Illinois 61801, United States

[‡]Department of Chemistry, Johns Hopkins University, Baltimore, Maryland 21218, United States

[§]Department of Chemistry, University of Wisconsin-Madison, Madison, Wisconsin 53706, United States

ABSTRACT: We report a solution NMR-based analysis of (16-mercaptohexadecyl)trimethylammonium bromide (MTAB) self-assembled monolayers (SAMs) on colloidal gold nanospheres (AuNSs) with diameters from 1.2 nm to 25 nm, and gold nanorods (AuNRs) with aspect ratios from 1.4 to 3.9. The chemical shift analysis of the proton signals from the solvent-exposed headgroups of bound ligands suggests that the headgroups are saturated on the ligand shell as the sizes of the nanoparticles increase beyond ~10 nm. Quantitative NMR shows that the ligand density of MTAB-AuNSs is size-dependent. Ligand density ranges from ~3 molecules per nm^2 for 25 nm particles, and up to 5 – 6 molecules per nm^2 in ~10 nm and smaller particles for *in situ* measurements of bound ligands; after I_2/I^- treatment to etch away the gold cores, ligand density ranges from ~2 molecules per nm^2 for 25 nm particles, and up to 4 – 5 molecules per nm^2 in ~10 nm and smaller particles. T_2 relaxation analysis shows greater hydrocarbon chain ordering and less headgroup motion as the diameter of the particles increases from 1.2 nm to ~13 nm. Molecular dynamics simulations of 4, 6, and 8 nm (11-mercaptoundecyl)trimethylammonium bromide (MUTAB) capped AuNSs confirm greater hydrophobic chain packing order and saturation of charged headgroups within the same spherical ligand shell at larger nanoparticle sizes and higher ligand densities. Combining the NMR studies and MD simulations, we suggest that the headgroup packing limits the ligand density, rather than the sulfur packing on the nanoparticle surface, for ~10 nm and larger particles. For MTAB-AuNRs, no chemical shift data nor ligand density data suggest that two populations of ligands that might correspond to side-ligands and end-ligands exist; yet T_2 relaxation dynamics data suggest that headgroup mobility depends on aspect ratio and absolute nanoparticle dimensions.

INTRODUCTION

Synthetic inorganic nanoparticles are often functionalized with an organic ligand shell, such as surfactants and polyelectrolytes, to improve colloidal stability in water and to facilitate their biological or environmental applications. The molecular composition and conformation of the ligand shell are crucial to the chemical and biological behavior of the nanoparticles.[1] Thiolated ligands are known to bind strongly to gold nanoparticles and form self-assembled monolayers (SAMs), which impart colloidal stability and desired functionality to the nanoparticles.[2] Surface functionality of SAMs on gold nanoparticles also plays an important role in nanoparticle cytotoxicity.[3] Spectroscopy and microscopy techniques, including UV-Vis[4], FTIR[5], XPS[5,6], TEM[7], and STM[8], have been explored to investigate the chemical environment of SAMs on gold nanoparticles. However, the determination of the ligand conformation at the molecular level is still challenging.[9]

Nuclear Magnetic Resonance (NMR)-based approaches provide great potential in elucidating the surface chemistry of ligand shells on nanoparticles in solution.[10] NMR has been used previously to investigate ligand shells on nanoparticles, to discriminate between bound and free ligands, to identify and quantify bound ligands, and to understand the binding mode of ligands and their dynamics.[7,11-16] Recent work has used NMR to infer protein orientation and conformation when bound to nanoparticle surfaces.[17,18] The majority of the reported NMR studies on small molecule SAMs on gold nanoparticles have been limited to isotropic spherical nanoparticles with diameters less than 6 nm. This is partly due to the relative low sensitivity of NMR, which requires a very concentrated nanoparticle sample. Typical gold nanoparticle colloidal solutions, for instance, are nM to μM in particles and the concentration limit for the larger nanoparticles is inherently lower because of their larger volumes. Moreover, ligands that are associated with larger nanoparticles experience significant line broadening, which can obscure peak assignments and integration. On the other hand, chemical shift, quantitative NMR, and T_2 relaxation experiments can provide crucial molecular-level information on the ligand shell in solution, which is inaccessible with other techniques.[10]

To overcome the aforementioned problems of using NMR to study ligand environment on larger nanoparticles, we synthesized (16-mercaptohexadecyl)trimethylammonium bromide (MTAB) and used MTAB SAMs on gold nanoparticles (AuNPs) as a model for solution NMR analysis (Scheme 1). MTAB-AuNPs are very stable in aqueous solution at very high particle concentrations, allowing the low sensitivity of NMR to be overcome.[19] The protons in the trimethylammonium head-

Scheme 1. A cartoon of the MTAB monolayer binding to a gold surface.

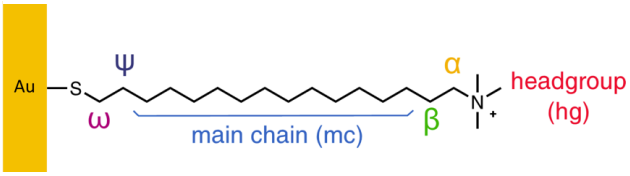

groups that are exposed to the solvent are the most mobile protons in the ligand, which makes them suffer the least from line broadening.[20] Furthermore, their chemical shift is ~ 2 ppm away from that of the interfering protons in the methylene main chain. Taken together, we choose these protons to infer ligand packing, mobility, and conformation.

It is known that the conformation of SAMs on gold nanoparticles less than 5 nm is highly dependent on the nanoparticle size and the surface curvature.[21] To further investigate the role of surface curvature on the ligand environment, and to examine the upper limit of the nanoparticle size that is suitable for NMR analysis, MTAB-AuNSs of sizes ranging from 1.4 nm to 25 nm were synthesized and analyzed by solution NMR. We used complementary MD simulations to investigate (11-mercaptoundecyl)trimethylammonium bromide (MUTAB), an analog of MTAB, on 4, 6 and 8 nm MTAB-AuNSs at different ligand densities. These simulations provide exquisite detail on the typical positions of the ligands at each of these three diameter sizes. Indeed, the NMR determined ligand packing order and headgroup mobility are seen to be commensurate with the structuring of the ligands seen in the MD simulations. For anisotropic nanoparticles such as gold nanorods (AuNRs), many experimental studies have inferred preferential reactions at the ends of the rods compared to the sides.[22,23] One key rationalization of anisotropic reactivity is a purported difference in ligand packing density on the ends vs. the sides of the rods; but no definitive proof, for instance by quantitative light-element imaging, has yet appeared.[23-28] To investigate the potential differences between ligands at the ends and at the sides of AuNRs, MTAB-AuNRs with aspect ratios ranging from 1.4 to 3.9 were synthesized, in which the ligand side population and end population might be different, and analyzed by solution NMR.

EXPERIMENTAL SECTION

Materials and instrumentation. All chemicals used in nanoparticle synthesis and functionalization, ligand synthesis, and NMR analysis (chloroauric acid, trisodium citrate, cetyltrimethylammonium bromide (CTAB), sodium borohydride, silver nitrate, hydrochloric acid (37%), 16-hexadecanediol, potassium thioacetate, acetyl chloride, hydrobromic acid (48 % aqueous solution), acetic anhydride, trimethyl amine solution in ethanol (4.2 M), anhydrous tetrahydrofuran, methanol, ethyl acetate, acetone, chloroform, maleic acid, iodine, potassium iodide, benzoic acid, $CDCl_3$ and D_2O) were obtained from Sigma-Aldrich and used as received.

After synthesis, nanoparticles were characterized by UV-Vis spectroscopy, dynamic light scattering (DLS), zeta potential analysis, and transmission electron microscopy (TEM). Concentrations were determined either according to published UV-Vis extinction coefficients or ICP-MS of digested solutions of known extinction.[29,30] UV−Vis spectra were measured with a Cary 5000 UV−Vis−NIR spectrophotometer (Agilent Technologies). DLS and zeta potentials were measured by a Malvern Zetasizer Nano-ZS (Malvern Panalytical Ltd.). Transmission electron microscopy (TEM) images of MTAB-AuNPs were collected by JEOL 2100 Cryo microscope (JEOL Ltd., Tokyo, Japan) in the Frederick Seitz Materials Research Laboratory, Central Facilities at the University of Illinois. Average sizes, lengths, widths, aspect ratios were determined by ImageJ software (National Institutes of Health). At least 300 particles were counted to determine the dimensions of each batch of MTAB-AuNPs. Inductively coupled plasma mass spectrometry (ICP-MS) was used to determine the gold concentration of each digested solution. A minimum of three measurements were taken for each batch of MTAB-AuNPs using a PerkinElmer Elan DRCe/NexION 350D ICP-MS instrument (PerkinElmer Inc.) in the Microanalysis Laboratory at School of Chemical Sciences at the University of Illinois.

MTAB-AuNPs were dispersed in deuterated water (99 atom % D). Released MTAB ligands were dissolved in $CDCl_3$ (99.8 atom % D). Nuclear magnetic resonance (NMR) spectra were acquired using a Varian Unity Inova narrow-bore 500 MHz (UI500NB) spectrometer and Varian Unity Inova narrow-bore 750 MHz (VNS750NB) spectrometer (Varian Inc.) at 298.15 K. Spectra were processed with MNova (Mestrelab Research). Chemical shifts are reported in parts per million (ppm) and are referenced to the residual proton solvent peak. Water suppression was not used. Spinning was turned off for all experiments. T_1 was measured by the inversion recovery method. T_2 was measured by introducing the Carr-Purcell-Meiboom-Gill (CPMG) pulse sequence and plotting the fitted peak area against decay time. The recycling time was set to 10 s, which is more than 5 times longer than the T_1 of the protons of interest. For quantitative NMR analysis, a known amount of maleic acid (with D_2O as solvent) or benzoic acid (with $CDCl_3$ as solvent) was added as internal standard and peak integrations were compared to this internal standard. Acquisition time was set to 2 seconds. Relaxation delay was set to at least 5 times of T_1 of the internal standard used (10 seconds for UI500NB and 15 seconds for VNS750NB).

MTAB ligand synthesis. MTAB ligands were synthesized by a modified reported 4-step method.[19] See supporting information for detailed synthesis procedures and ^1H NMR, ^{13}C NMR and MS characterization (Figure S4-S6). MTAB slowly oxidized over time to its disulfide (Figure 3, Figure S5). Both thiol and disulfide form SAMs on gold nanoparticles.[31]

MTAB-AuNP synthesis. In a typical synthesis, citrate- or CTAB-stabilized gold nanoparticles are first synthesized and then MTAB ligands are exchanged at elevated temperature in excess. See supporting information for detailed synthesis procedures.

MTAB-AuNP dissolution. MTAB-AuNPs were treated with I_2/I^- by a modified procedure.[32] In a typical reaction, 100 μL of MTAB-AuNPs from the NMR measurement was added to 2 mL aqueous solution containing 0.5 M I_2 and 2 M KI under gentle stirring. After 48 hours, $CHCl_3$ was added to the solution to extract the released ligands (1 mL each, three times). The extracted ligands were dried by rotary evaporation before 600 μL of $CDCl_3$ was added. A known amount of benzoic acid was added as internal standard. Quantitative NMR was used to determine the concentration of released ligands.

Molecular dynamics simulations. Computational structures of AuNSs at sizes 4, 6, 8 nm in diameter were constructed through a sequence of steps: placing gold atoms at least two atomic radii apart within a sphere, heating the system to 1400 K, slowly cooling to 300K, and equilibrating at 300K. We used (11-mercaptoundecyl)trimethylammonium bromide (MUTAB)

as a simplified model for MTAB. The OPLS-AA force field is used to model the interactions of MUTAB ligands.[33] Previous simulation studies of SAMs on gold surfaces with chain lengths in the range of 9-20 carbons have shown that the hydrophobic chain packing dominates the structure with a negligible effect of the headgroup chemistry on the positioning of headgroups.[34,35] The interaction between the gold atoms is modeled using a Lennard-Jones potential initially with the parameters specified by Heinz and co-workers.[36] The Lennard-Jones parameters for the interaction potential between gold atoms employed in simulations of MUTAB functionalization onto gold were subsequently adjusted so that the gold-carbon parameters, after applying geometric mixing rules, fit those developed by Landman and co-workers to model alkane adsorption onto gold surfaces.[37] The adjusted parameter for $\varepsilon_{Au\text{-}Au}$ is 1.55 kcal/mol and for $\sigma_{Au\text{-}Au}$ is 2.629 Å.

To simulate ligand attachment, a Morse potential was used for the interaction between sulfur and gold atoms, using the parameterization of Ghorai and Glotzer.[34] MUTAB ligands were placed with sulfur atoms near the nanoparticle surface with the AuNS fixed at the center of the simulation box, and simulations were run for 0.1 ns at 300 K. We subsequently defined harmonic bonds between sulfur atoms and their nearest gold atoms. The system was equilibrated for 2 ns at 300 K, and then heated for 3 ns at 400 K, following the protocol of Luedtke and Landman.[38] The system was re-equilibrated for 10 ns at 300 K and until a convergence in the average tilt angle of ligands was reached (Figure S16). Production simulations for an additional 10 ns were then run to obtain data for analysis with samples collected once every picosecond, and are used in constructing the figures.

Packmol was used to construct initial configurations for AuNS synthesis and to distribute MUTAB ligands on the AuNS surface at 4.0 and 6.0 molecules per nm^2 densities.[39] All simulations were propagated using LAMMPS at 2 femtoseconds per timestep.[40] Periodic boundary conditions were employed with a 10 Å cutoff for pairwise interactions at constant NVE condition—that is, number of atoms N, volume V, and energy E. A Langevin thermostat with a damping constant of 10 ps^{-1} provided energy dissipation and maintained the average energy vis-à-vis effective temperature. The particle-particle particle-mesh (PPPM) method was used to calculate electrostatic interactions with explicit bromide counterions included to neutralize each ligand. The relative permittivity was set to 80.1 so as to represent water. Box sizes were chosen so that the total bromide concentration was 0.136 M.

RESULTS

MTAB-AuNP synthesis and characterization. TEM images and UV-Vis spectra of the obtained MTAB-AuNPs confirm that the particles are reasonably monodisperse (Figures 1 & 2). The TEM size distributions and UV-Vis spectra of MTAB-AuNPs are consistent with reports from the literature.[29,41,42] MTAB-capped gold nanospheres (MTAB-AuNSs) remain stable for at least five rounds of centrifugation and redispersion.[19] After MTAB ligand exchange, it is difficult to directly centrifuge gold nanospheres with diameters less than 10 nm. Therefore, we purified these nanospheres by first adding acetone and then centrifuging the solution, washing precipitates twice with acetone before vacuum-drying, and redispersing in D_2O. The localized surface plasmon resonances (LSPR) of the obtained MTAB-AuNSs red-shift from 521 nm to 529 nm as the size increases from 4.8 nm to 25.4 nm (Figure 2). For NMR, "mini" gold nanorods (MTAB-AuNRs) were prepared according to a recently published seed-mediated growth procedure.[26] The longitudinal LSPR of MTAB-AuNRs shift from 527 nm to 770 nm as the aspect ratio of the nanorods increases from 1.4 ± 0.3 to 3.9 ± 0.6 (Figure 2). The residual unreacted seeds (~1.5 nm) were found to complicate the NMR analysis and were removed by multiple rounds of centrifugation. The characterization data for the library of MTAB-coated gold nanoparticles are provided in supporting information (Table S1 & S2).

NMR analysis of MTAB-AuNSs. Figure 3 shows the ^{1}H NMR spectra obtained for MTAB-AuNSs with diameters ranging from 1.2 nm to 25.0 nm. Only two broadened proton signals can be differentiated for MTAB ligands on nanoparticles: an NMR resonance centered at about 3 ppm (containing mostly

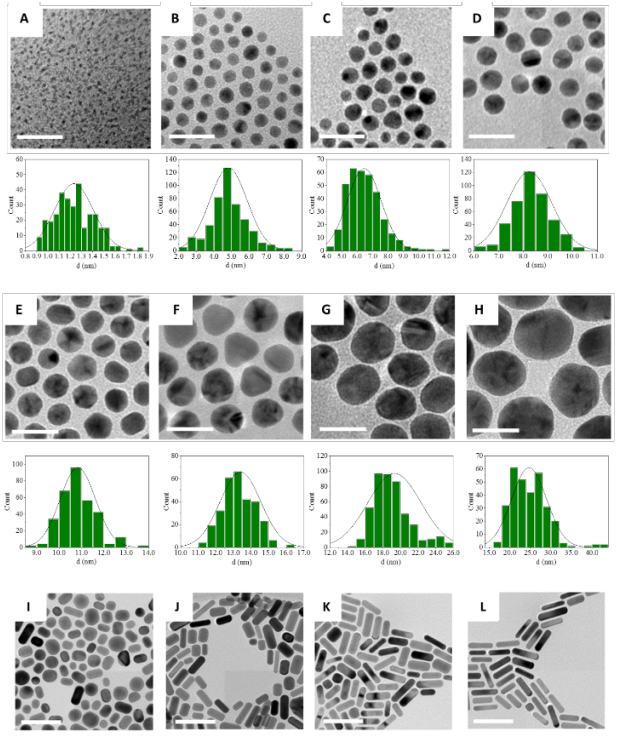

Figure 1. TEM images and histograms of MTAB-AuNSs and MTAB-AuNRs. For spheres, mean diameters with one standard deviation from the mean are: A: 1.2 ± 0.3 nm. B: 4.8 ± 1.1 nm. C: 6.4 ± 1.1 nm. D: 8.2 ± 0.9 nm. E: 10.8 ± 0.8 nm. F: 13.4 ± 1.2 nm. G: 19.3 ± 3.0 nm. H: 25.0 ± 4.4 nm. Scale bars: 20 nm. Aspect ratios of MTAB-AuNRs are: I: 1.4 ± 0.3. J: 2.3 ± 0.6. K: 3.2 ± 0.7. L: 3.9 ± 0.6. Scale bars: 50 nm.

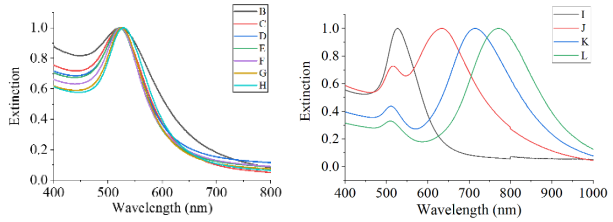

Figure 2. Normalized UV-Vis spectra of MTAB-AuNSs (left) and MTAB-AuNRs (right) of various dimensions. The UV-Vis spectrum of MTAB-AuNSs (1.2 ± 0.3 nm, A in Figure 1) is not included because their size is too small to support surface plasmons. B: 4.8 ± 1.1 nm. C: 6.4 ± 1.1 nm. D: 8.2 ± 0.9 nm. E: 10.8 ± 0.8 nm. F: 13.4 ± 1.2 nm. G: 19.3 ± 3.0 nm. H: 25.0 ± 4.4 nm. Aspect ratios of MTAB-AuNRs: I: 1.4 ± 0.3. J: AR: 2.3 ± 0.8. K: AR: 3.2 ± 0.9. L: AR: 3.9 ± 0.7.

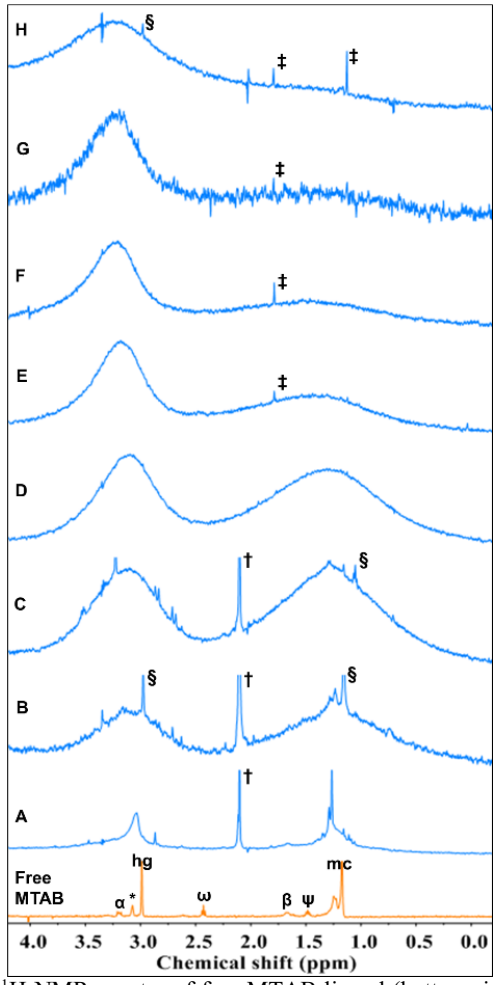

Figure 3. ^{1}H NMR spectra of free MTAB ligand (bottom, in orange) and MTAB-AuNSs of given diameters in D_2O. A: 1.2 ± 0.3 nm. B: 4.8 ± 1.1 nm. C: 6.4 ± 1.1 nm. D: 8.2 ± 0.9 nm. E: 10.8 ± 0.8 nm. F: 13.4 ± 1.2 nm. G: 19.3 ± 3.0 nm. H: 25.0 ± 4.4 nm. The concentration of each sample is given in Table S1. Detailed ^{1}H NMR spectrum of free MTAB is shown in Figure S5. †: Residual acetone signal. ‡: Signal from impurities from plastic centrifugation tubes. §: Residual CTAB signal. *: Signal from the head group protons in MTAB disulfide. The other sharp NMR peaks come from unknown impurities.

headgroup protons) and an even broader NMR resonance centered at about 1.3 ppm (containing mostly main chain protons). Headgroup protons, farther away from the core, suffer less broadening than main chain protons; as a result, the headgroup proton resonance is less broad than those of the main chain protons.[20,43,44] The headgroup proton resonance and main chain proton resonance in MTAB-AuNSs (gold core 1.2 ± 0.3 nm) show a mono-exponential diffusion decay with the same diffusion coefficient of 38 μm^2/s measured by diffusion-ordered spectroscopy (DOSY), which yield a hydrodynamic diameter of 13 nm calculated by the Stokes-Einstein equation. Hydrodynamic sizes of the other particles studied in this paper are measured by dynamic light scattering (DLS) and are provided in Table S1 & S2 in the supporting information. No overlaping sharp peak indicate that free MTAB ligands are at low enough concentrations to not be detected by NMR. The main chain proton signals gradually broaden into the baseline as the size of nanoparticles increases, whereas the headgroup proton signals can still be detected for nanoparticles of sizes up to 25 nm. ^{1}H NMR spectra of 25 nm MTAB-AuNSs were also measured by another NMR

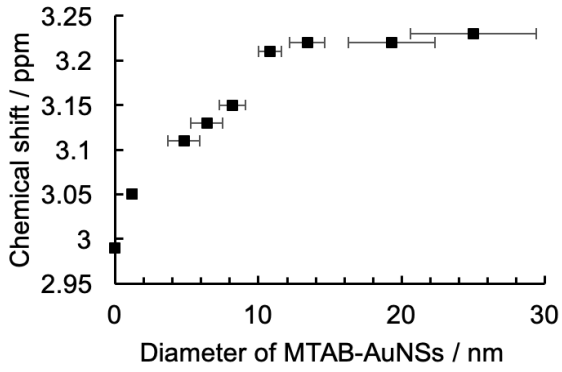

Figure 4. Dependence of the chemical shift of the headgroup protons of bound MTAB as a function of gold nanosphere diameter. Error bars for chemical shifts are smaller than the squares. Free MTAB is at 0 diameter.

instrument with 3-fold higher proton sensitivity (Figure S7). The headgroup peak integration compared to the internal standard is almost the same, but the main chain proton peak integration is significantly higher, which suggests that the headgroup protons can still be fully detected by ^{1}H NMR. MTAB-AuNSs with a diameter of 33 nm were prepared with a particle concentration of about 100 nM, but the headgroup proton signals were already broadened into the baseline under the same measurement conditions, we conclude that for MTAB-AuNSs, ~25 nm is the largest size that is suitable for NMR analysis (Figure S8). Concentrations of the samples used are provided in Table S1 in the supporting information.

Chemical shift. Chemical shifts of the headgroup proton signals depend on the size of the gold nanospheres (Figure 4). The chemical shift of the headgroup protons in the free MTAB ligands is 2.99 ppm. We observe a gradual downfield shift in the headgroup proton signals from 3.05 ppm to 3.23 ppm as the size of the nanospheres increases from 1.2 nm to 10.8 nm. Then the chemical shift plateaus after the size of nanoparticles reach beyond 10.8 nm.

The chemical shift of thiol ligands is known to be not only determined by their chemical structures but also by their neighboring ligands.[8] For single moiety ligand shell such as MTAB, the chemical shift of headgroup protons is dependent on the MTAB packing density: the number and/or distance of neighboring positively charged headgroups affect the electron density of headgroup protons. The ^{1}H NMR signals (in D_2O) of the MTAB head group protons shift downfield from 2.99 ppm to 3.07 ppm when forming MTAB disulfide (Figure 3, Figure S5).

The trend in chemical shift is similar to what is observed for the MTAB analog CTAB as a function of concentration: as CTAB transition from single molecules to premicelles, to spherical micelles, and finally to rod-shaped micelles in water upon increasing concentration, the headgroup proton signals shift downfield from 2.98 ppm to 3.11 ppm (Figure S9).[45] For MTAB on gold nanospheres, the similar trend in chemical shift from 2.99 ppm to 3.23 ppm suggests that MTAB packing density increases as particle size increases, up to 10.8 nm. Beyond

10.8 nm, MTAB headgroups are saturated on the gold nanoparticle surface. The headgroups might form a more ordered structure on the particle surface compared to CTAB micelles.

Ligand density. Since the headgroup protons can be fully detected by ^{1}H NMR for sizes up to 25 nm, we can potentially use the headgroup proton peaks as a probe to quantify the ligands on nanoparticles by quantitative ^{1}H NMR analysis using an internal standard. Maleic acid was used as an internal standard because its proton signals do not overlap with the MTAB headgroup protons and it does not interact with MTAB ligands. The headgroup proton peaks are fitted so that the α proton contribution is excluded in the calculation. The peak area (PA) from Gaussian-Lorentzian line fitting is used for NMR quantification. Equation 1 is used to calculate the total molar concentration of MTAB ligands $coMTAB_{bound}u$

$$coMTAB_{bound}u = \frac{2}{9} \times \frac{PAoMTAB\ head\ groupu}{PAoMaleic\ acidu} \times coMaleic\ acidu \quad o1u$$

where $coMaleic\ acidu$ is the molar concentration of maleic acid molecules, and the 2/9 ratio reflects the relative number of protons in the two molecules. For MTAB-AuNSs with sizes larger than 12 nm, the molar concentration of gold nanoparticles $coAuNSu$ was obtained by UV-Vis spectroscopy through reported extinction coefficients in the literature.[30] For MTAB-AuNSs with sizes smaller than 12 nm, the molar concentration of gold nanoparticles $coAuNSu$ was obtained by a combination of mass concentration $\gamma oAuu$ from ICP-MS and the radius of gold nanoparticles r determined by TEM according to Equation 2

$$coAuNSu = \frac{\gamma oAuu}{VoAuNSu \times N_A} = \frac{\gamma oAuu}{\frac{4}{3}\pi r^3 \times \rho_{Au} \times N_A} \quad (2)$$

where ρ_{Au} is the density of gold and N_A is the Avogadro constant. Equation 3 is used to calculate the total gold surface area SA_T from $coAuNSu$ and r.

$$SA_T = coAuNSu \times 4\pi r^2 \times V \quad (3)$$

where V is the volume of the AuNS solution. Finally, Equation 4 is used to calculate ligand density d:

$$d_{bound} = \frac{coMTAB_{bound}u \times V}{SA_T} = \frac{1}{3}\rho_{Au}N_A \times \frac{coMTAB_{bound}u \times r}{\gamma oAuu} \quad o4u$$

One might argue that since the headgroup proton peaks are broad, the processing of the NMR spectra such as baseline correction and peak fitting may cause integration errors. Therefore, we also used an indirect method to quantify the ligand density. I_2/I^- was used to etch the gold core in MTAB-AuNPs and release the surface bound MTAB ligands. Compared to other gold etchant such as aqua regia that may oxidize MTAB ligands and cyanides that form side products such as thiocyanide (Figure S11), I_2/I^- is much milder and no side reactions were observed from NMR (Figure S12). Since MTAB and its disulfide do not dissolve in water under room temperature after being released, $CHCl_3$ was used to extract the released the ligands. We found that no more free ligands can be extracted after 48 hours of reaction. Benzoic acid was used as an internal standard because its proton signals do not overlap with the MTAB headgroup protons and it does not interact with MTAB ligands.

Similar to ligand quantification of surface bound ligands discussed above, Equation 5 is used to calculated the molar concentration of released MTAB ligands

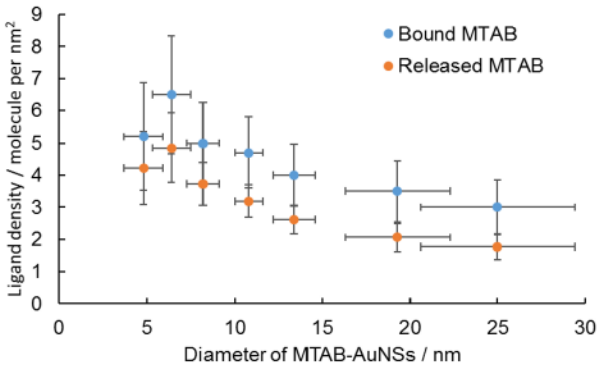

Figure 5. Dependence of ligand density of the headgroup protons of bound MTAB as a function of gold nanoparticle diameter. Blue dots: data from in situ quantitative NMR integration relative to a maleic acid internal standard. Orange dots: data from experiments in which the gold was digested and free ligands were quantified relative to a benzoic acid internal standard.

$$coMTAB_{released}u = \frac{1}{9} \times \frac{PAoMTAB\ head\ groupu}{PAoBenzoic\ acidu} \times coBenzoic\ acidu \quad o5u$$

The ligand density determined by released ligands can be obtained by equation 6

$$d_{released} = \frac{coMTAB_{released}u}{coMTAB_{bound}u} \times d_{bound} \quad o6u$$

The error bars can be calculated by

$$\frac{\sigma_d}{d} = \sqrt{o\frac{\sigma_{coMTABu}}{coMTABu}u^2\ d\ o\frac{\sigma_{\gamma oAuu}}{\gamma oAuu}u^2\ d\ o\frac{\sigma_r}{r}u^2} \quad o7u$$

For ligand quantification of surface bound MTAB, the coefficient of variation in $coMTABu$ from qNMR is estimated to be 20%, and 10% for $\gamma oAuu$ from ICP-MS analysis. The coefficient of variation of gold nanoparticle radius r can be determined by TEM size distribution. For ligand quantification of released MTAB, the coefficient of variation in $coMTABu$ from qNMR is estimated to be 10%.

Figure 5 shows the relationship between the ligand density and the sizes of the nanospheres. The error bars in Figure 5 combine that of particle size heterogeneity from TEM, gold content quantification from ICP-MS measurement and of the ligand quantification from quantitative NMR as described above. The MTAB ligand density is size dependent from both methods: the ligand density decreases as the size of the nanoparticles increases, from ~5-6 MTAB molecules per nm^2 to ~3 MTAB molecules per nm^2 if we directly quantify the bound MTAB ligands, or from ~4-5 MTAB molecules per nm^2 to ~2 molecules per nm^2 if we quantify the released MTAB ligands after I_2/I^- treatment, as nanosphere size increases from 4.8 nm to 25.0 nm. The 1.2 nm spheres showed some aggregation under TEM (more than 50 nm), which is not detectable by NMR; but this sample heterogeneity reduced our confidence in the accuracy for these very small particles (Figure S10).

T_2 relaxation and peak width. T_2 relaxation, or spin-spin relaxation, is a measure of the decay constant for the component of magnetization perpendicular to the external magnetic field.[10] T_2 can be measured by introducing the Carr-Purcell-Meiboom-Gill (CPMG) pulse sequence.[46,47] In this method, an initial 90-degree pulse is applied, followed by a series of 180-degree spin echo pulses. The decay time between the spin echo and the next 180-degree pulse was varied, and T_2 can be obtained by fitting

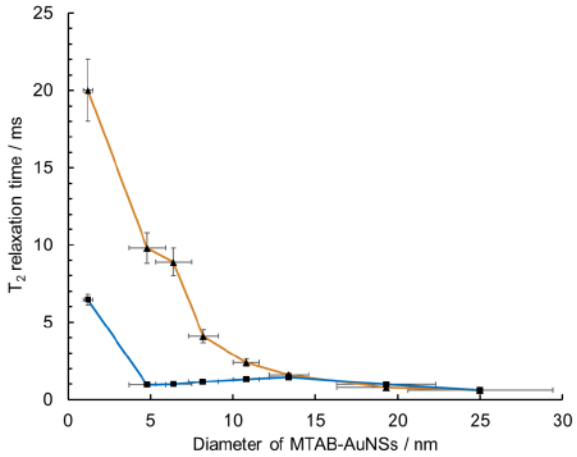

Figure 6. Dependence of T_2 (orange line) and T_2^* (blue line) of the MTAB headgroup protons as a function of gold nanoparticle diameter.

the magnetization (peak area from Gaussian-Lorentzian fitting) to a mono-exponential function:

$$M_{xy}(t) = M_{xy}(0)e^{-t/T_2} \quad (8)$$

T_2 relaxation is caused by transient magnetic fields which are usually due to molecular motion. For bound ligands, it has been established that the isotropic tumbling of the entire nanoparticle, the motion of a ligand with respect to the nanoparticle and to each other all contribute to T_2.[10] As the size of the nanoparticle increases, the slower they tumble and the motion of the ligand decreases due to the increasing hydrocarbon chain packing. Therefore, T_2 of the bound ligands shortens as the size of the nanoparticle increases. For a homogeneous system, T_2 is inversely proportional to the peak width (*pw*, linewidth at half height):

$$T_2 = 1/(\pi \times pw) \quad (9)$$

Due to the heterogeneity within the NMR instrumentation and sometimes within the sample itself, T_2 calculated by peak width, which is referred to T_2^*, is almost always larger than the T_2 determined by the CMPG pulse sequence. Equation 9 suggests that protons with slower molecular motion show broader NMR peaks. However, the relationship between the peak width of the MTAB headgroup protons and nanoparticle size is more complicated than we expected: the fitted peak width decreased from 334 Hz to 216 Hz, or T_2^* increased from 0.9 ms to 1.5 ms, as the size of the nanoparticle increased from 4.8 nm to 13.4 nm (Figure S13). On the other hand, T_2 relaxation times determined by the CMPG pulse sequence decreased from 20 ms to 0.6 ms as the size of nanoparticles increased from 1.2 nm all the way to 25 nm. If we compare T_2^* and T_2, their difference is negligible after 13.4 nm (Figure 6).

We attribute the T_2 and T_2^* differences for nanoparticles smaller than 13.4 nm to the heterogeneous chemical environment of the headgroups. The observed NMR resonance envelope is composed of a distribution of sharper resonances caused by different chemical environment of headgroups.[44] The incomplete hydrocarbon chain packing creates free volume in space available for headgroups at high surface curvatures. As the size of the nanoparticle increases, the degree of hydrocarbon chain packing increases, so that there is less space available for headgroups to move, and less differences between T_2 and T_2^* are observed. When the size of the nanoparticles reaches 13.4 nm and beyond, T_2 and T_2^* differences are less than 0.3 ms, which suggests that other problems that may also contribute to observed differences in T_2 and T_2^*, such as magnetic field inhomogeneity and temperature gradient across sample, are negligible compared to headgroup inhomogeneity. Thus, chemical environment of the MTAB headgroups can be considered homogeneous as the size of the nanoparticles increases beyond 13.4 nm. Overall, the trend is that the headgroup motion decreases as particle size increases.

Molecular dynamics simulations. We used molecular dynamics simulations to study the structure of the MUTAB ligand layer on 4, 6, and 8 nm AuNSs at ligand densities of 4.0 and 6.0 molecules nm^{-2}—the minimum and maximum in the range of ligand densities determined for 4 and 8 nm AuNSs (Figure 5). Representative images of MUTAB-AuNSs show that MUTAB forms islands on the nanoparticle surface (Figure 7). The formation of ligand islands is attributed to the competition between hydrophobic chain packing and the free volume in space available per ligand particularly at high surface curvatures.[34,35,48] To quantify the structural changes in the MUTAB layer as a function of AuNS size and ligand density, we calculated the radial distribution function, $g(r)$, between the AuNS center of mass and nitrogen atoms in the headgroup of MUTAB (Figure 8) and the $g(r)$ between all pairs of nitrogen atoms (Figure 9). The $g(r)$'s were obtained using histograms with bin sizes of 0.1 Å averaged over 5000 frames per trajectory for five trajectories per AuNS size and ligand density and normalized by the annular volume. The $g(r)$'s for individual trajectories are available in the Supporting Information (Figure S14 & S15).

At a ligand density of 4.0 molecules nm^{-2}, the $g(r)$ between the AuNS center and MUTAB headgroups for 4 nm AuNSs shows peaks that appear near the surface (Figure 8). This suggests that a significant number of ligands lie along the AuNS surface. As the AuNS size increases and curvature decreases, there are fewer ligands lying on the nanoparticle surface, as shown by the disappearance of the peaks near the surface, designated as 2 nm, 3 nm, and 4 nm from the nanoparticle center for 4, 6, and 8 nm AuNSs, respectively (Figure 8). The hump

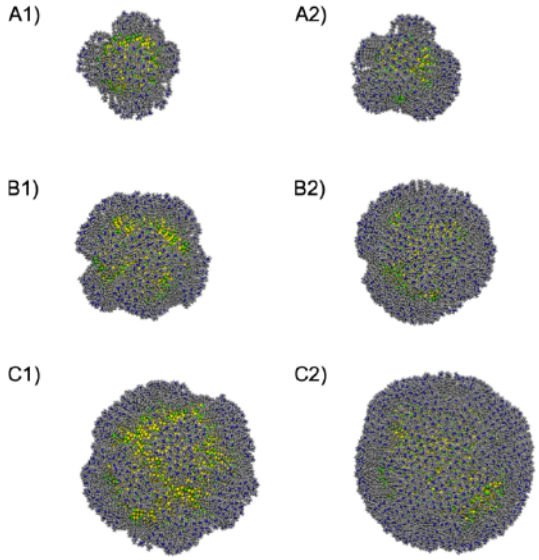

Figure 7. Simulation snapshots of MUTAB-AuNSs with the following size and ligand density: Rows A, B and C correspond to 4 nm, 6 nm, and 8 nm diameters, respectively; and Columns 1 and 2 correspond to 4.0 molecules nm^{-2} and 6.0 molecules nm^{-2} ligand densities. Gold atoms are shown in yellow, sulfur in green, carbon in gray, hydrogen in white, and nitrogen in blue. Bromide counterions are removed for clarity.

between peaks at the surface and the major peak also disappears as the nanoparticle size increases. The greater spatial distribution of MUTAB headgroups on smaller AuNSs is attributed to an increase in chain packing disorder due to greater free volume per ligand and the greater tilt of chains particularly on the edges of the ligand islands as ligands pack along AuNSs of higher surface curvature.[34,48,49] Further, the disappearance of the hump and the increase in magnitude of the major peak suggest that MUTAB ligands on 8 nm AuNSs are more ordered, standing more upright with decreased tilt due to greater hydrophobic chain packing on the nanoparticle surface. At a higher ligand density of 6.0 molecules nm^{-2}, the $g(r)$ between the AuNS center and MUTAB headgroups reveals a single major peak for all AuNS sizes (Figure 8). The $g(r)$'s show a more pronounced tail near the surface of 4 nm AuNSs and sharper peaks for the larger AuNSs, signifying greater chain packing order at lower surface curvatures and higher ligand densities.

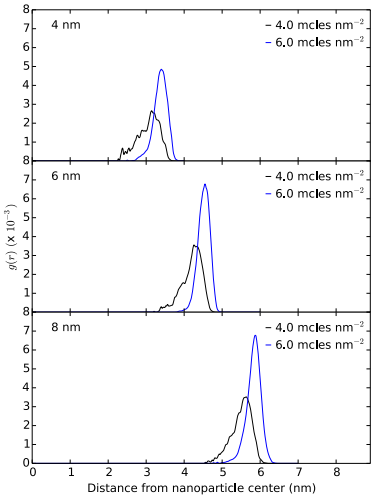

Figure 8. Radial distribution function, $g(r)$, between the nanoparticle center of mass for 4, 6, and 8 nm AuNSs and the nitrogen atoms of MUTAB at ligand densities of 4.0 and 6.0 MUTAB molecules nm^{-2}.

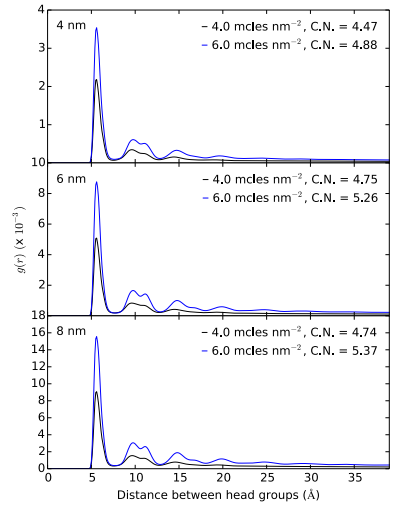

Figure 9. Radial distribution function, $g(r)$, between all pairs of nitrogen atoms in the headgroup of MUTAB at ligand densities of 4.0 and 6.0 MUTAB molecules nm^{-2}. The coordination number (C.N.) of MUTAB headgroups is determined by taking the integral under the first peak in each $g(r)$.

Measuring the distance between all pairs of nitrogen atoms, we find that the nearest neighbor for each MUTAB headgroup is 5.4 Å away independent of AuNS size and ligand density (Figure 9). The coordination number of each headgroup increases and approaches the hexagonal packing limit of 6.0 with both increasing AuNS size and ligand density. Figure 8 and 9 combined suggest that for smaller AuNSs and at lower ligand densities, there is a greater spatial distribution of headgroups relative to the AuNS surface with smaller coordination number per headgroup. For larger AuNSs and at higher ligand densities, a higher coordination number per charged headgroup and greater chain packing order lead to the accumulation of high charge density within the same spherical shell relative to the

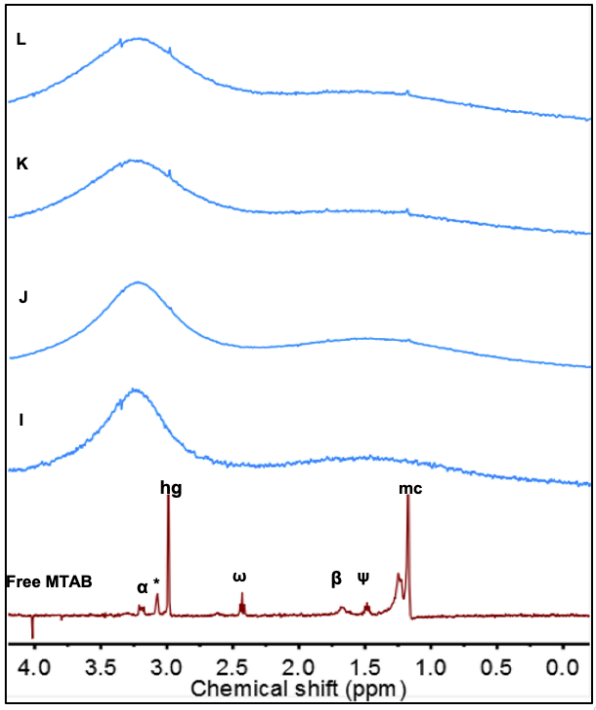

Figure 10. ^{1}H NMR spectra of free MTAB ligands and MTAB-AuNRs of various aspect ratios. I: 1.4 ± 0.3. J: 2.3 ± 0.6. K: 3.2 ± 0.7. L: 3.9 ± 0.6. The short and long axis of the nanorods are provided in Table S1.

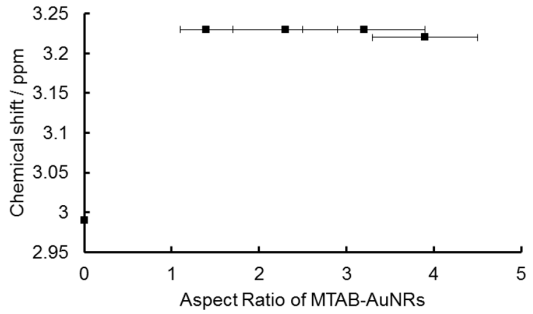

Figure 11. Chemical shift of the headgroup protons of bound MTAB on gold nanorods as a function of gold nanorod aspect ratio. Free MTAB is at "0" aspect ratio.

nanoparticle center, which could explain the downfield shifts in headgroup protons observed under such conditions by NMR experiments.

NMR analysis of MTAB-AuNRs. Compared to the ligand environments on gold nanospheres, MTAB ligands on gold nanorods potentially have two different chemical environments: at the sides and the ends of the nanorods. It is believed that the curved surface at the ends of the gold nanorods causes the hydrocarbon chains to be less densely packed.[23] We undertook NMR studies to assess the ability of NMR to distinguish between ligands bound to different spatial locations on these anisotropic colloids.

To minimize the undesired line broadening, "mini" gold nanorods were prepared for studying the differences of ligand environment between the ends and sides of the rods.[29] Figure 10 shows the ^{1}H NMR spectra obtained for MTAB-AuNRs with aspect ratios ranging from 1.4 to 3.9. Concentrations of the samples used are provided in Table S2. Similar to MTAB-AuNSs, the headgroup proton peaks in MTAB-AuNRs are also broadened and shifted to downfield with no overlapping sharp peaks, indicating that MTAB ligands are bound to the gold surface and no free ligands were observed, while the main chain peaks are so broadened that they disappear into the baseline.

Chemical shift. Larger aspect ratios of gold nanorods ought to produce larger side/end ratios of ligand populations. If the chemical environments or headgroup packing of bound ligands were sufficiently different on the sides and ends of rods, we might expect to see two headgroup peaks for the bound MTAB ligands. However, we observe similar chemical shifts of the headgroup protons for all the MTAB-AuNRs studied (Figure 11) and those for MTAB-AuNSs larger than 10 nm. According to the chemical shift study of MTAB-AuNSs, the headgroups of MTAB on both the sides and ends of the gold nanorods can be considered to be tightly packed despite the curvature at the ends of the gold nanorods; therefore, by NMR there is no evidence for distinguishable end and side environments for the ligands.

Ligand density. The MTAB ligand density on gold nanorods was determined by quantitative NMR studies with two methods similar to MTAB-AuNSs discussed above. For MTAB-AuNRs with aspect ratios larger than 2, the molar concentration of gold nanorods $coAuNRu$ was obtained by UV-Vis spectroscopy through reported longitudinal extinction coefficients in the literature.[29] For MTAB-AuNRs with aspect ratios smaller than 2, the molar concentration of gold nanorods $coAuNRu$ was obtained by a combination of mass concentration $\gamma oAuu$ from ICP-MS and length l and width w of gold nanorods determined by TEM. Equation 10 and equation 11 was used to calculate the total gold surface area SA_T and gold nanorod volume $VoAuNRu$ from $coAuNRu$ and the width w and length l of gold nanorods .

$$SA_T = coAuNRu \times \left(\pi w^2 + \pi wol - wu\right) \times V = coAuNRu \times \pi wl \times V \quad (10)$$

$$VoAuNRu = \frac{4}{3}\pi o\frac{w}{2}u^3 + \pi w^2 ol - wu = \pi w^2 o\frac{l}{4} - \frac{w}{12}u \quad o11u$$

Ligand density of MTAB-AuNRs calculated from ^{1}H NMR of bound ligands can be obtained by equation 12.

$$d_{bound} = \rho_{Au}N_A \times \frac{coMTAB_{bound}u \times wo\frac{1}{4} - \frac{w}{12l}u}{\gamma oAuu} \quad o12u$$

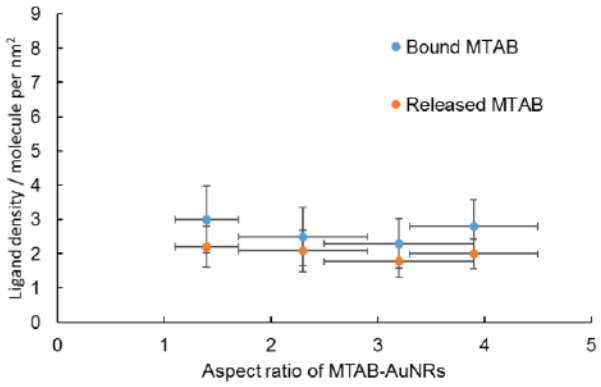

Figure 12. Ligand density for MTAB bound to gold nanorods as a function of gold nanorod aspect ratio. Blue dots: data from in situ quantitative NMR integration relative to a maleic acid internal standard. Orange dots: data from experiments in which the gold was digested and free ligands were quantified relative to a benzoic acid internal standard. From equation 12, ligand density d is found to be $\rho_{Au}N_A \times \frac{coMTABu \times wo\frac{1}{4} - \frac{w}{12l}u}{\gamma oAuu}$. Therefore, according to error propagation, error bars can be calculated by $\sigma_d = \rho_{Au}N_A \times$

$$\sqrt{\left(\frac{coMTABuw}{4\gamma oAuu}\right)^2 To\frac{\sigma_{coMTABu}}{coMTABu}u^2 d \left(\frac{\sigma_{\gamma oAuu}}{\gamma oAuu}u\right)^2 d \left(\frac{\sigma_w}{w}\right)^2 B}$$

$$w\sqrt{d \frac{w^2}{9l^2} o\frac{coMTABuw}{4\gamma oAuu}u^2 To\frac{\sigma_{coMTABu}}{coMTABu}u^2 d o\frac{\sigma_{\gamma oAuu}}{\gamma oAuu}u^2 d 4o\frac{\sigma_w}{w}u^2 d o\frac{\sigma_l}{l}u^2 B}$$

For ligand quantification of surface bound MTAB, the coefficient of variation in $coMTABu$ from qNMR is estimated to be 20%, and 10% for $\gamma oAuu$ from ICP-MS analysis. The coefficient of variation of length l and width w of gold nanorods can be determined by TEM. For ligand quantification of released MTAB, the coefficient of variation in $coMTABu$ from qNMR is estimated to be 10%.

Similar to MTAB-AuNSs, ligand density was calculated after MTAB ligands were released with I_2/I^- treatment; error bar calculations are given in the caption of Figure 12. Figure 12 shows the ligand density values calculated from both methods. The error bars in Figure 12 combine that of particle size heterogeneity from TEM, gold content quantification from ICP-MS measurement and of the ligand quantification as described above. The ligand density values range from 2.3 to 3.0 molecules per nm^2

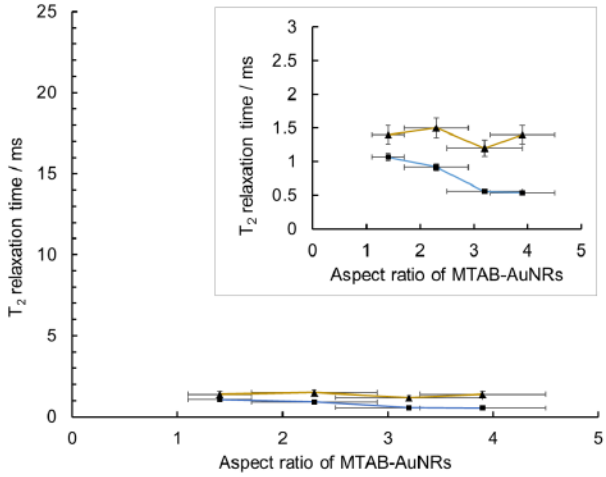

Figure 13. Dependence of T_2 (orange) and T_2^* (blue) of the MTAB head group protons as a function of the aspect ratio of gold nanorods.

of gold surface if we directly quantify the bound MTAB ligands, and 1.8 to 2.2 molecules per nm^2 of gold surface if we quantify the released MTAB ligands. No significant differences across gold nanorods of different aspect ratios are observed, which suggests that the distances between the sulfur atoms in surface bound MTAB are similar between the sides and ends of the gold nanorods.

T_2 relaxation and peak width. Similar to MTAB-AuNSs, T_2 and T_2^* were also compared for MTAB-AuNRs of different aspect ratios (Figure 13). Mono-exponential decays were observed for MTAB-AuNRs instead of bi-exponential decay that might have been expected for differential packing at the ends of sides of rodlike objects (Figure S26-S29). As the aspect ratio increases, the difference between T_2 and T_2^* increases. From the NMR analysis of MTAB-AuNSs, the chemical environment of the MTAB ligands is highly dependent on the surface curvature. The observed trend in T_2 and T_2^* differences for rods is correlated with the decrease in the rod width (from 12.1 ± 2.4 nm to 7.4 ± 1.0 nm as AR increases from 1.4 to 3.9). Taken together, the relaxation data suggest that MTAB headgroups are more heterogeneous on gold nanorods with higher aspect ratios.

DISCUSSION

The literature of self-assembled monolayers of thiols on gold is vast.[2] The majority of studies that focus on the details of ligand density and conformation are on flat gold surfaces or on colloidal gold nanoparticles of less than ~6 nm diameter. For instance, Häkkinen et al. interpreted the ^{1}H spectra of p-mercaptobenzoic acid capped 1.5 nm gold clusters in solution in terms of the special ligand environments on the cluster surface by multidimensional NMR, DFT calculations, and MD simulations.[50] Murray et al. investigated dodecanethiolate capped gold nanoparticles of 1.5 to 5.2 nm in diameter by studying the methylene stretching modes in infrared spectroscopy (IR), and showed that ligands adopted a highly ordered conformation on ~4 nm gold nanoparticles in the solid phase. They also analyzed gold nanoparticles by ^{1}H NMR and showed that NMR signals are broader as the diameter of the nanoparticles increases from 1.5 nm to 5.2 nm, and the peak broadening causes difficulties in interpretation.[21] For particles larger than 5 nm, Castner et al. used ATR-FTIR to investigate the compactness of –COOH terminated SAMs on 14 nm, 25 nm, and 40 nm gold nanoparticles in the solid phase, and showed that C_{16}COOH-SAMs are well-ordered on 14 nm gold nanoparticles.[5] To our knowledge, there are no reports of using NMR to study SAMs on gold nanoparticles larger than ~6 nm. The advantage of using solution-phase NMR for detailed ligand characterization is that measurements can be made *in situ* in aqueous solution, the most relevant environment for the many biological applications of these particles; the disadvantage is the low sensitivity of NMR.[10]

To overcome the main disadvantage of NMR, colloidal gold nanoparticle solutions in this study were prepared at concentrations ~100 times compared to those of typical measurements, without aggregation. The highly charged and somewhat bulky headgroups of the MTAB ligands helped contribute to this increase in colloidal stability as well as providing a convenient NMR handle (the solvent-accessible quaternary ammoniums).

For MTAB-AuNSs, the chemical shift analysis of the headgroups, ligand density analysis and T_2 relaxation analysis allow us to infer the packing and mobility of the headgroups and the sulfur atoms respectively in MTAB ligands when bound to gold nanoparticles of various diameters. One key result is the ligand density and the packing of headgroups are not necessarily correlated. If we consider Figures 4, 5, and 6, we learn that as the particle diameter increases, the chemical environment of the ligand headgroup more and more resembles, and may even pack denser than that of a well-packed micelle (Figure 4); yet the ligand density is largest for the smaller nanoparticles (< 10 nm), and is smallest for the largest nanoparticles (Figure 5). We are forced to conclude, then, that for the smaller nanoparticles, the ligands must be more disordered and mobile, which agrees with the T_2 relaxation analysis (Figure 6). The experimental data agree well with the conclusions from the MD simulations reported above. The pair correlation functions, $g(r)$, in Figures 8 and 9 show that increasing the nanoparticle size leads both to increased ordering of the headgroups and decreased direct contact between the headgroups and the nanoparticle surface. The key result from the simulations, illustrated in Figure 7, is the existence of ligand islands with increased propensity in the smaller nanoparticles that leads to closer headgroup packing between proximal ligands than would be seen if they were uniformly distributed across the nanoparticle. The consensus interpretation from both the experiments and simulations is summarized in Scheme 2, illustrating how the conformation of MTAB SAMs on gold nanoparticles changes according to the nanoparticle size.

Ligand densities of MTAB on gold nanospheres and nanorods of different diameters/aspect ratios were quantified by NMR in two independent ways: direct peak integration, relative to a maleic acid standard, of bound ligands; and peak integration of released ligands after iodine/iodide etching of the gold cores, relative to a benzoic acid standard. The numerical values follow the same trend with sizes (Figures 5 and 12), but the averages differ by ~30-50%, with the *in situ* measurements systematically larger than the digested values. Incomplete digestion and/or the ligand losses in the purification process in the digestion method would cause those calculated ligand density values to be smaller than the direct, *in situ* method. The obtained peak area values after line fitting and baseline correction in the *in situ* method may include small contributions from MTAB non-head group protons, which would cause these calculated values to be a bit larger than the "true" ligand density. However, we also note that the error bars in both measurements do overlap for each sample.

There are many reports of ligand density on SAMs on gold nanoparticles in the literature, using many different methods. Some reports suggest that ligand density is size-dependent, similar to what we found. As early as 1987, Nuzzo and Dubois et al. studied methanethiolate SAMs on Au(111) surface under ultra-high vacuum (UHV) conditions, and reported a surface coverage of 0.33, or a ligand density of 4.65 molecules per nm^2, by XPS.[51] Murray et al. studied dodecanethiol capped 2.4 nm gold nanoclusters, and found out that surface coverage is double this value (0.66), compared to ligands on flat Au(111) surface, combining SAXS and elemental analysis. Their analysis suggested that the high surface curvature relieves the steric crowding and/or the reactivity of Au atoms on the surface.[43] Mirkin et al. quantified thiolated oligonucleotides on gold nanoparticles of 10 to 200 nm diameters by fluorescence. They also observed that smaller nanoparticle sizes exhibited larger ligand densities than larger particles, but the absolute values of ligand density are smaller than the ones we report here, due to large size of the oligonucletides.[52]

Other reports, however, suggest that the ligand density on gold nanoparticles is size-independent. Lämmerhofer et al.

studied ligand coverage of C3, C11, C16 COOH-SAMs on gold nanoparticles of 13 nm to 26 nm in diameter by plotting the ratio of gold to sulfur amount determined by ICP-MS to nanoparticle diameter. A linear relationship was observed, implying that the ligand density is size-independent.[53] Millstone et al. also analyzed the ligand density of C8 and C11 COOH terminated SAMs on gold nanoparticles of 13 nm and 31 nm in diameter using NMR to quantify digested ligands and ICP-MS to quantify gold content, and the results also suggest that ligand density is size-independent.[54]

These apparently conflicting reports can be reconciled by considering the volume of the terminal headgroup on the SAM. The spherical volume occupied by sulfur, COO^-, and $N(CH_3)_3^+$ is 7.24, 8.18, and 82.4 $Å^3$, respectively. For ligands with bulky headgroups and flexible linkers, such as MTAB and DNA, headgroup size controls ligand density. At small particle sizes, headgroup jamming is avoided by altered conformations at full ligand coverage, but at sufficiently large sizes where the headgroups are saturated on the ligand shells, headgroup sizes and surface curvature control ligand density (Scheme 2). The computer images captured in Figure 7 and the statistically significant structure found through the radial distribution functions of Figure 9 reveal that MTAB headgroups transition from islands to uniform coverage with increasing ligand density, and the onset occurs at lower ligand density with increasing AuNSs size. For headgroups that have a similar or smaller size than sulfur bound to the gold surface, such as carboxylic acids, ligand density is size-independent (Scheme 3).

Scheme 2. Scheme showing the MTAB conformation and packing as a function of nanoparticle size.

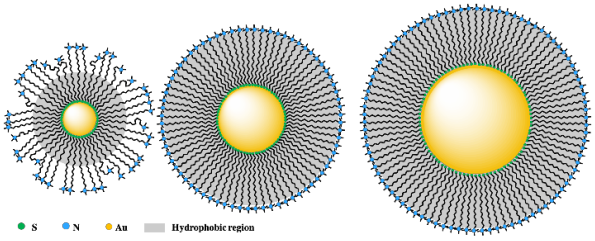

Scheme 3. Scheme showing for ligands that have headgroups that are similar or smaller in size than sulfur, ligand density should be independent of particle size.

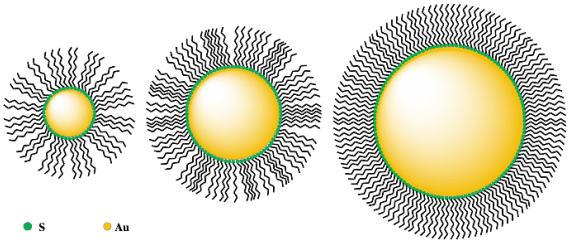

CONCLUSION

In this work, we have shown that solution NMR spectroscopy is a robust analytical tool for determining the structural conformation of the ligand shell in situ of both isotropic and anisotropic nanoparticles. In parallel, molecular dynamics simulations provided an atomic resolution of the equilibrium structure and the transition of the ligand coverage from small to large diameter AuNSs. By studying the chemical shifts, ligand densities, and T_2 relaxation behaviors in concert with simulations, we are able to systematically demonstrate the ligand conformation of MTAB-AuNSs of sizes from 1.2 nm to 25 nm and MTAB-AuNRs of aspect ratios from 1.4 to 3.9 *in situ* in aqueous solution.

ASSOCIATED CONTENT

Supporting Information

The Supporting Information is available free of charge on the ACS Publications website.

The Supporting Information contains procedures of MTAB synthesis and characterization, MTAB-AuNP synthesis, characterization of MTAB-AuNP library, supporting NMR spectra, supporting TEM images, supporting figures for MTAB-AuNP dissolution, peak width analysis of MTAB-AuNSs, supporting figures for MD simulations, and T_2 decay curves for MTAB-AuNPs.

AUTHOR INFORMATION

Corresponding Author

* murphycj@illinois.edu

Author Contributions

All authors have given approval to the final version of the manuscript.

Funding Sources

This work was supported by National Science Foundation under the Center for Sustainable Nanotechnology (CSN), CHE-1503408. The CSN is part of the Centers for Chemical Innovation Program.

Notes

The authors declare no competing financial interest.

ACKNOWLEDGMENT

This work was supported by National Science Foundation under the Center for Sustainable Nanotechnology (CSN), CHE-1503408. The CSN is part of the Centers for Chemical Innovation Program. We gratefully thank the Frederick Seitz Materials Research Laboratory, Central Facilities at the University of Illinois for TEM characterization. We thank Dr. Olson Dean and Dr. Lingyang Zhu from the NMR facilities at the School of Chemical Sciences in University of Illinois for helpful discussions regarding T_2 relaxation experiments. We thank the Microanalysis Laboratory at School of Chemical Sciences at the University of Illinois for ICP-MS analysis. Computing resources were provided in part by the National Science Foundation through XSEDE resources under grant number CTS090079 and by the Maryland Advanced Research Computing Center.

REFERENCES

(1). Albanese, A.; Tang, P. S.; Chan, W. C. W. The effect of nanoparticle size, shape, and surface chemistry on biological systems. *Annu. Rev. Biomed. Eng.* **2012**, 14, 1-16.

(2). Love, J. C.; Estroff, L. A.; Kriebel, J. K.; Nuzzo, R. G.; Whitesides, G. M. Self-assembled monolayers of thiolates on metals as a form of nanotechnology. *Chem. Rev.* **2005**, 105, 1103-1170.

(3). Kim, S. T.; Saha, K.; Kim, C.; Rotello, V. M. The role of surface functionality in determining nanoparticle cytotoxicity. *Acc. Chem. Res.* **2013**, 46, 681-691.

(4). Weisbecker, C. S.; Merritt, M. V.; Whitesides, G. M. Molecular self-assembly of aliphatic thiols on gold colloids. *Langmuir* **1996**, 12, 3763−3772.

(5). Techane, S. D.; Gamble, L. J.; Castner, D. G. Multitechnique characterization of self-assembled carboxylic acid-terminated alkanethiol monolayers on nanoparticle and flat gold surfaces. *J. Phys. Chem. C* **2011**, 115, 9432-9441.

(6). Torelli, M. D.; Putans, R. A.; Tan, Y.; Lohse, S. E.; Murphy, C. J.; Hamers, R. J. Quantitative determination of ligand densities on nanomaterials by X-ray photoelectron spectroscopy. *ACS Appl. Mater. Interfaces* **2015**, 7, 1720-1725.

(7). Azubel, M.; Koivisto, J.; Malola, S.; Bushnell, D.; Hura, G. L.; Koh, A. L.; Tsunoyama, H.; Tsukuna, T.; Pettersson, M.; Häkkinen, H.; Kornberg, R. D. Electron microscopy of gold nanoparticles at atomic resolution. *Science* **2014**, 345, 909-912.

(8). Liu, X.; Yu, M.; Kim, H.; Mameli, M.; Stellacci, F. Determination of monolayer-protected gold nanoparticle ligand–shell morphology using NMR. *Nat. Commun.* **2012**, 3, 1182.

(9). Colangelo, E.; Comenge, J.; Paramelle, D.; Volk, M.; Chen, Q.; Lévy, R. Characterizing self-assembled monolayers on gold nanoparticles. *Bioconjugate Chem.* **2016**, 28, 11-22.

(10). Zeger, H.; Martins, J. C. A solution NMR toolbox for characterizing the surface chemistry of colloidal nanocrystals. *Chem. Mater.* **2013**, 25, 1211-1221.

(11). Moreels, I.; Justo, Y.; De Geyter, B.; Haustraete, K.; Martins, J. C.; Hens, Z. Size-tunable, bright, and stable PbS quantum dots: a surface chemistry study. *ACS Nano* **2011**, 5, 2004−2012.

(12). Zhang, Y.; Fry, C. G.; Pedersen, J. A.; Hamers, R. J. Dynamics and morphology of nanoparticle-linked polymers elucidated by nuclear magnetic resonance. *Anal. Chem.* **2017**, 89, 12399-12407.

(13). Cros-Gagneux, A.; Delpech, F.; Nayral, C.; Cornejo, A.; Coppel, Y.; Chaudret, B. Surface chemistry of InP quantum dots: a comprehensive study. *J. Am. Chem. Soc.* **2010**, 132, 18147−18157.

(14). Boles, M. A.; Ling, D.; Hyeon, T.; Talapin, D. V. The surface science of nanocrystals. *Nat. Mater.* **2016**, 15, 141-153.

(15). Badia, A.; Lennox, R. B.; Reven, L. A dynamic view of self-assembled monolayers. *Acc. Chem. Res.* **2000**, 33, 475-481.

(16). Zelakiewicz, B. S.; de Dios, A. C.; Tong, Y. ^{13}C NMR spectroscopy of $^{13}C_1$-labeled octanethiol-protected Au nanoparticles: shifts, relaxations, and particle-size effect. *J. Am. Chem. Soc.* **2003**, 125, 18-19.

(17). Lin, W.; Insley, T.; Tuttle, M. D.; Zhu, L.; Berthold, D. A.; Král, P.; Rienstra, C. M.; Murphy, C. J. Control of protein orientation on gold nanoparticles. *J. Phys. Chem. C* **2015**, 119, 21035-21043.

(18). Fawzi, N. L.; Ying, J.; Ghirlando, R.; Torchia, D. A.; Clore, G. M. Atomic-resolution dynamics on the surface of amyloid-β protofibrils probed by solution NMR. *Nature* **2011**, 480, 268.

(19). Vigderman, L.; Manna, P.; Zubarev, E. R. Quantitative replacement of cetyl trimethylammonium bromide by cationic thiol ligands on the surface of gold nanorods and their extremely large uptake by cancer cells. *Angew. Chem. Int. Ed.* **2012**, 124, 636-641.

(20). Riccardi, L.; Gabrielli, L.; Sun, X.; De Biasi, F.; Rastrelli, F.; Mancin, F.; De Vivo, M. Nanoparticle-based receptors mimic protein-ligand recognition. *Chem* **2017**, 3, 92-109.

(21). Hostetler, M. J.; Wingate, J. E.; Zhong, C. J.; Harris, J. E.; Vachet, R. W.; Clark, M. R.; Londono, J. D.; Green, S. J.; Stokes, J. J.; Wignall, G. D.; Glish, G. L.; Porter, M. D.; Evans, N. D.; Murray, R. W. Alkanethiolate gold cluster molecules with core diameters from 1.5 to 5.2 nm: core and monolayer properties as a function of core size. *Langmuir* **1998**, 14, 17-30.

(22). Sau, T. K.; Murphy, C. J. Self-assembly patterns formed upon solvent evaporation of aqueous cetyltrimethylammonium bromide-coated gold nanoparticles of various shapes. *Langmuir* **2005**, 21, 2923–2929.

(23). Hinman, J. G.; Eller, J. R.; Lin, W.; Li, J.; Li, J.; Murphy, C. J. Oxidation state of capping agent affects spatial reactivity on gold nanorods. *J. Am. Chem. Soc.* **2017**, 139, 9851-9854.

(24). Xu, L.; Kuang, H.; Xu, C.; Ma, W.; Wang, L.; Kotov, N. A. Regiospecific plasmonic assemblies for in situ Raman spectroscopy in live cells. *J. Am. Chem. Soc.* **2012**, 134, 1699-1709.

(25). Thomas, K. G.; Barazzouk, S.; Ipe, B. I.; Joseph, S. S.; Kamat, P. V. Uniaxial plasmon coupling through longitudinal self-assembly of gold nanorods. *J. Phys. Chem. B* **2004**, 108, 13066-13068.

(26). Caswell, K. K.; Wilson, J. N.; Bunz, U. H.; Murphy, C. J. Preferential end-to-end assembly of gold nanorods by biotin−streptavidin connectors. *J. Am. Chem. Soc.* **2003**, 125, 13914-13915.

(27). Wang, F.; Cheng, S.; Bao, Z.; Wang, J. Anisotropic overgrowth of metal heterostructures induced by a site-selective silica coating. *Angew. Chem. Int. Ed.* **2013**, 52, 10344-10348.

(28). Kim, J. Y.; Han, M. G.; Lien, M. B.; Magonov, S.; Zhu, Y.; George, H.; Norris, T. B.; Kotov, N. A. Dipole-like electrostatic asymmetry of gold nanorods. *Sci. Adv.* **2018**, 4, e1700682.

(29). Chang, H. H.; Murphy, C. J. Mini gold nanorods with tunable plasmonic peaks beyond 1000 nm. *Chem. Mater.* **2018**, 30, 1427-1435.

(30). Haiss, W.; Thanh, N. T.; Aveyard, J.; Fernig, D. G. Determination of size and concentration of gold nanoparticles from UV−Vis spectra. *Anal. Chem.* **2007**, 79, 4215-4221.

(31). Häkkinen, H. The gold–sulfur interface at the nanoscale. *Nat. Chem.* **2012**, 4, 443.

(32). Templeton, A. C.; Hostetler, M. J.; Kraft, C. T.; Murray, R. W. Reactivity of monolayer-protected gold cluster molecules: steric effects. *J. Am. Chem. Soc.* **1998**, 120, 1906-1911.

(33). Jorgensen, W. L.; Maxwell, D. S.; Tirado-Rives, J. Development and testing of the OPLS all-atom force field on conformational energetics and properties of organic liquids. *J. Am. Chem. Soc.* **1996,** 118, 11225-11236.

(34). Ghorai, P. K.; Glotzer, S. C. Molecular dynamics simulation study of self-assembled monolayers of alkanethiol surfactants on spherical gold nanoparticles. *J. Phys. Chem. C* **2007,** 111, 15857-15862.

(35). Bolintineanu, D. S.; Lane, J. M. D.; Grest, G. S. Effects of functional groups and ionization on the structure of alkanethiol-coated gold nanoparticles. *Langmuir* **2014,** 30, 11075-11085.

(36). Heinz, H.; Vaia, R. A.; Farmer, B. L.; Naik, R. R. Accurate simulation of surfaces and interfaces of face-centered cubic metals using 12-6 and 9-6 Lennard-Jones potentials. *J. Phys. Chem. C* **2008,** 112, 17281-17290.

(37). Xia, T. K.; Ouyang, J.; Ribarsky, M. W.; Landman, U. Interfacial alkane films. *Phys. Rev. Lett.* **1992,** 69, 1967-1970.

(38). Luedtke, W. D.; Landman, U. Structure and thermodynamics of self-assembled monolayers on gold nanocrystallites. *J. Phys. Chem. B* **1998,** 102, 6566-6572.

(39). Martínez, L.; Andrade, R.; Birgin, E. G.; Martínez, J. M. Packmol: a package for building initial configurations for molecular dynamics simulations. *J. Comput. Chem.* **2009,** 30, 2157-2164.

(40). Plimpton, S. Fast parallel algorithms for short-range molecular-dynamics. *J. Comput. Phys.* **1995,** 117, 1-19.

(41). Sau, T. K.; Murphy, C. J. Room temperature, high-yield synthesis of multiple shapes of gold nanoparticles in aqueous solution. *J. Am. Chem. Soc.* **2004**, 126, 8648–8649.

(42). Orendorff, C. J.; Murphy, C. J. Quantitation of metal content in the silver-assisted growth of gold nanorods. *J. Phys. Chem. B* **2006**, 110, 3990-3994.

(43). Terrill, R. H.; Postlethwaite, T. A.; Chen, C. H.; Poon, C. D.; Terzis, A.; Chen, A.; Hutchison, J. E.; Clark, M. R.; Wignall, G.; Londono, J. D.; Superfine, R.; Falvo, M.; Johnson Jr, C. S.; Samulski, E. T.; Murray, R. W. Monolayers in three dimensions: NMR, SAXS, thermal, and electron hopping studies of alkanethiol stabilized gold clusters. *J. Am. Chem. Soc.* **1995**, 117, 12537–12548.

(44). De Roo, J.; Yazdani, N.; Drijvers, E.; Lauria, A.; Maes, J.; Owen, J. S.; Van Driessche, I.; Niederberger, M.; Wood, V.; Martins, J. C.; Infante, I.; Hens, Z. Probing solvent–ligand interactions in colloidal nanocrystals by the NMR line broadening. *Chem. Mater.* **2018**, 30, 5485-5492.

(45). Cui, X.; Mao, S.; Liu, M.; Yuan, H.; Du, Y. Mechanism of surfactant micelle formation. *Langmuir* **2008**, 24, 10771-10775.

(46). Carr, H. Y.; Purcell, E. M. Effects of diffusion on free precession in nuclear magnetic resonance experiments. *Phys. Rev.* **1954**, 94, 630−638.

(47). Meiboom, S.; Gill, D. Modified spin-echo method for measuring nuclear relaxation times. *Rev. Sci. Instrum.* **1958**, 29, 688−691.

(48). Ahn, Y.; Saha, J. K.; Schatz, G. C.; Jang, J. Molecular dynamics study of the formation of a self-assembled monolayer on gold. *J. Phys. Chem. C* **2011,** 115, 10668-10674.

(49). Frederick, M. T.; Achtyl, J. L.; Knowles, K. E.; Weiss, E. A.; Geiger, F. M. Surface-amplified ligand disorder in CdSe quantum dots determined by electron and coherent vibrational spectroscopies. *J. Am. Chem. Soc.* **2011,** 133, 7476-7481.

(50). Salorinne, K.; Malola, S.; Wong, O. A.; Rithner, C. D.; Chen, X.; Ackerson, C. J.; Häkkinen, H. Conformation and dynamics of the ligand shell of a water-soluble Au_{102} nanoparticle. *Nat. Commun.* **2016**, 7, 10401.

(51). Nuzzo, R. G.; Zegarski, B. R.; Dubois, L. H. Fundamental studies of the chemisorption of organosulfur compounds on gold (111). Implications for molecular self-assembly on gold surfaces. *J. Am. Chem. Soc.* **1987**, 109, 733-740.

(52). Hill, H. D.; Millstone, J. E.; Banholzer, M. J.; Mirkin, C. A. The role radius of curvature plays in thiolated oligonucleotide loading on gold nanoparticles. *ACS Nano* **2009**, 3, 418-424.

(53). Hinterwirth, H.; Kappel, S.; Waitz, T.; Prohaska, T.; Lindner, W.; Lämmerhofer, M. Quantifying thiol ligand density of self-assembled monolayers on gold nanoparticles by inductively coupled plasma–mass spectrometry. *ACS Nano* **2013**, 7, 1129-1136.

(54). Smith, A. M.; Marbella, L. E.; Johnston, K. A.; Hartmann, M. J.; Crawford, S. E.; Kozycz, L. M.; Seferos, D. S.; Millstone, J. E. Quantitative analysis of thiolated ligand exchange on gold nanoparticles monitored by ^{1}H NMR spectroscopy. *Anal. Chem.* **2015**, 87, 2771-2778.

Authors are required to submit a graphic entry for the Table of Contents (TOC) that, in conjunction with the manuscript title, should give the reader a representative idea of one of the following: A key structure, reaction, equation, concept, or theorem, etc., that is discussed in the manuscript. Consult the journal's Instructions for Authors for TOC graphic specifications.

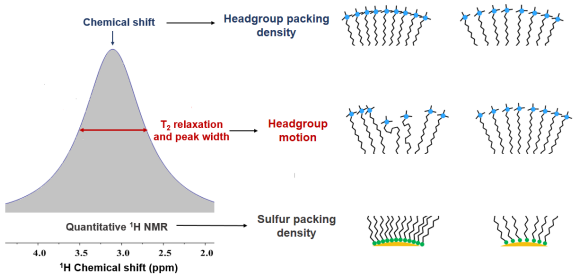

Insert Table of Contents artwork here